



# SRM UNMANNED AERIAL VEHICLE

Journal Paper for AUVSI SUAS 2019

SRM Institute of Science of Technology

INDIA



## ABSTRACT

This document serves as an account of the technical development of SRM Institute of Science & Technology's SRM-UAV towards an Unmanned Aerial System capable of autonomous flight, obstacle avoidance, imagery and air delivery for AUVSI's SUAS 2019. The team has taken steps to achieve a multi-disciplinary engineering solution to be a part of the aerial delivery technology of the future. Safety, efficiency and accuracy have been the cornerstones for the teams development towards the system.



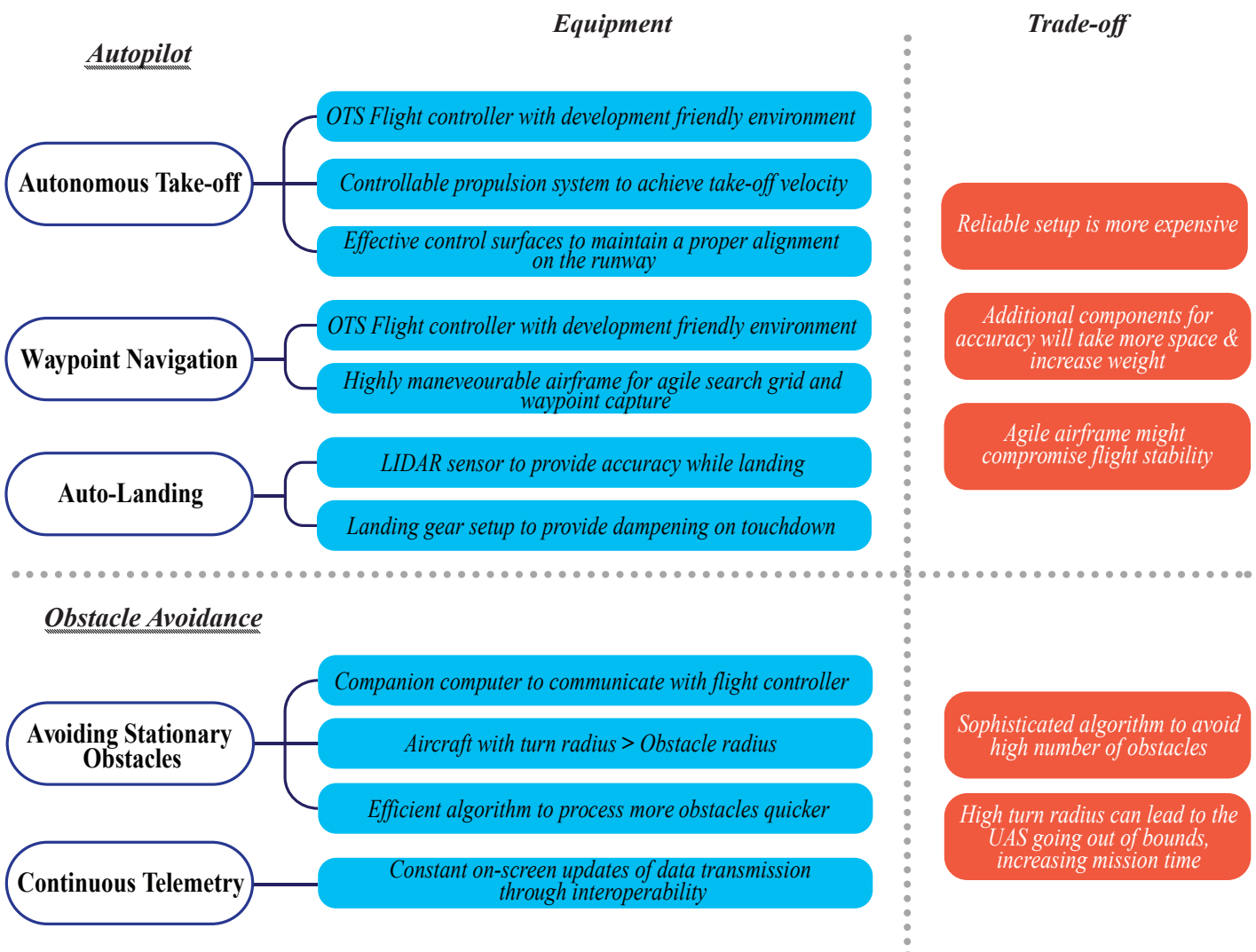
## 1. SYSTEMS ENGINEERING APPROACH

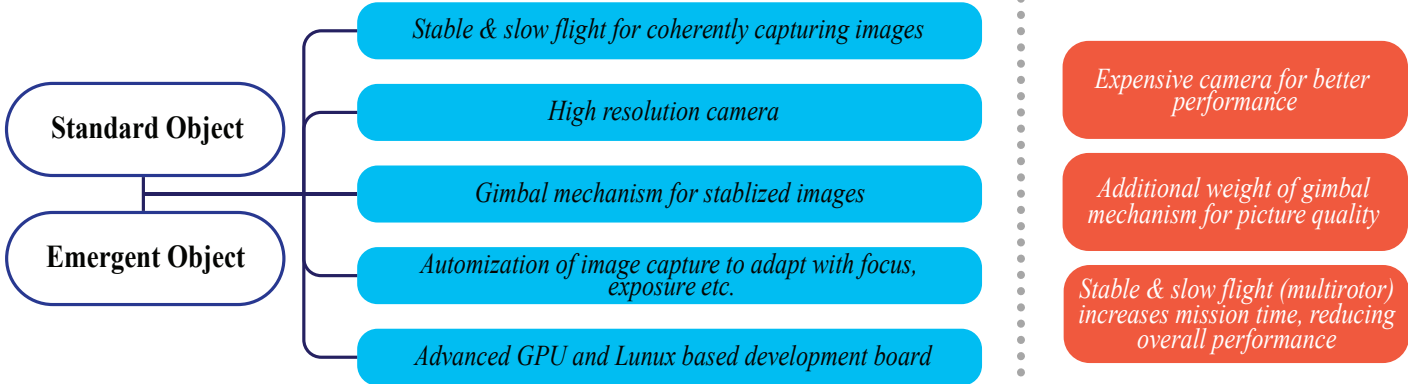
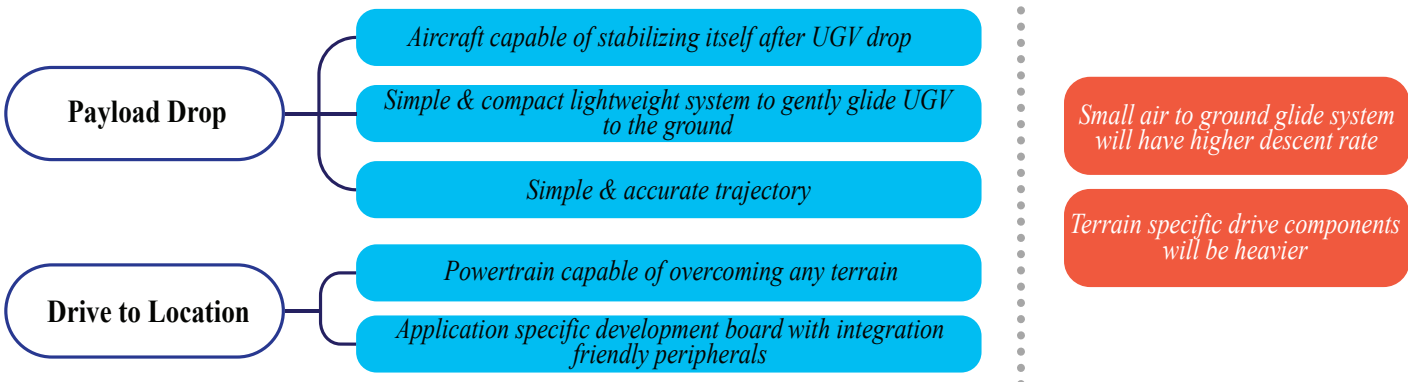
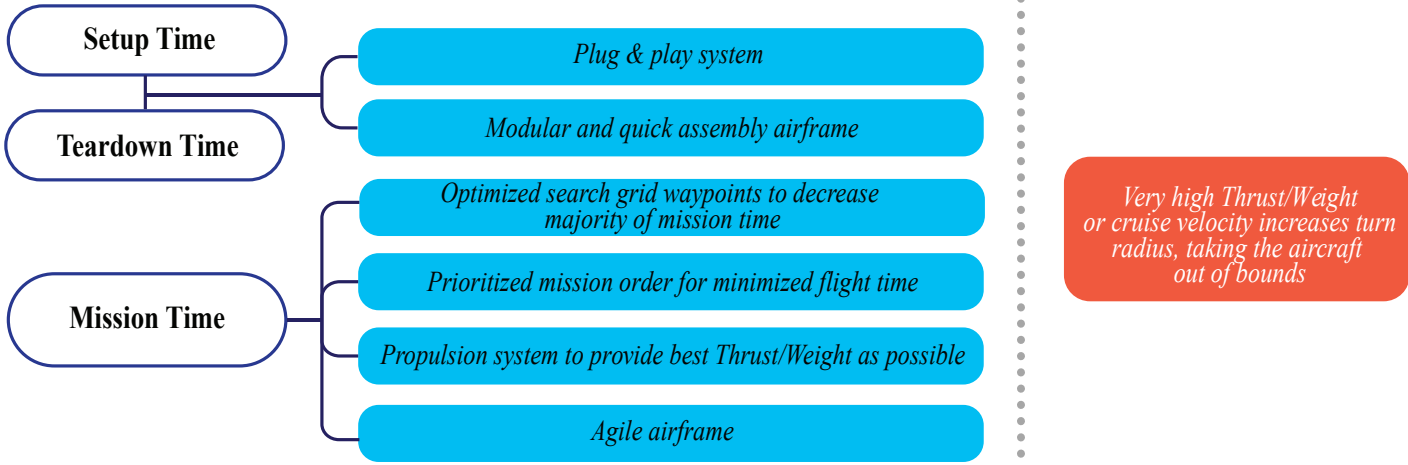
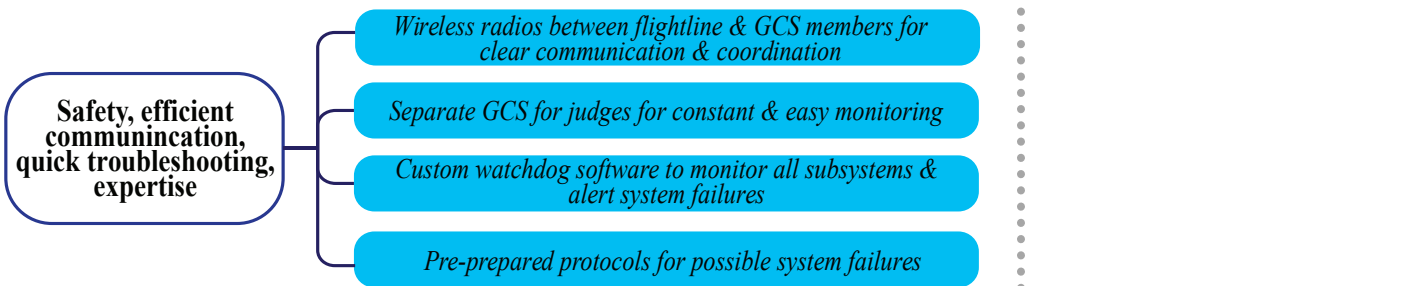
The Orca was holistically engineered to provide an end-to-end solution for modern delivery drones that fly autonomously while avoiding architectural obstacles, processing images and dropping package-equipped unmanned ground vehicles to customers and the technology developed is being validated through the platform of the AUVSI SUAS 2019 competition. Being aimed towards being an end user product, the UAS needs to fulfil requirements of being safe to fly, easy to operate, reliably accurate and cost effective. The technical requirements of achieving the desired performance for the AUVSI SUAS 2019 have been illustrated in the following sections.

### 1.1 Mission Requirement Analysis

The following chart describes the equipments and trade offs of all missions and their sub-missions that were considered during the system engineering approach. For the Autonomous Flight mission to be carried out successfully, the UAS should be capable of taking off, landing and capturing waypoints accurately and safely. To fulfil this, a reliable off the shelf flight controller with readily available hardware peripherals was desired while not being very expensive. An agile and maneuverable airframe was required to capture the waypoints with ease without compromising the aircraft's stability. Additional sensors were incorporated for augmented auto-landing accuracy with a landing gear setup capable of providing damped and safe touchdown. In addition to these, a companion computer with an efficient algorithm and minimum overhead calculations is required to communicate with the flight controller in order

to avoid the stationary obstacles. Moreover, the airframe has to be designed with a performance envelope such that it can turn around the obstacle without colliding with it. A telemetry system integrated with the flight controller is desired for communicating all airborne information to the ground station without any interruptions. The mission also demands a high resolution camera to capture images clearly without pixelating from the high operating altitude and subsequently identifying them accurately. To do so, an advanced GPU is favourable to run heavy image processing algorithms. From the previous years experiences, it was understood that an adaptive and automated system was needed to be developed and integrated with the image processing system to perform the image capturing activity in accordance to the change in lighting conditions. An optimised search grid pattern is desirable that covers the entire search area while not increasing the mission time and having a stable flight regime. An additional camera stabilisation system to stabilise the camera during aircraft turbulences and vibrations is imperative to a successful ODCL mission. In order to deliver the package successfully, the package-equipped UGV needs to be dropped to the ground gently with an accurate and simple trajectory to minimise structural damage. Moreover, the airframe should be dynamically stable to stabilise itself after the detachment of the UGV load. The UGV design process needs to consider the drive mechanism and their corresponding sensors in order to have the efficacy of driving over any kind of terrain autonomously. Multiple simulations of the entire mission need to be performed to improve the overall timeline and the



**ODCL****Air Delivery****Timeline****Operational Excellence****Figure 1:** Mission requirement analysis flowchart



## 1.2 Design Rationale

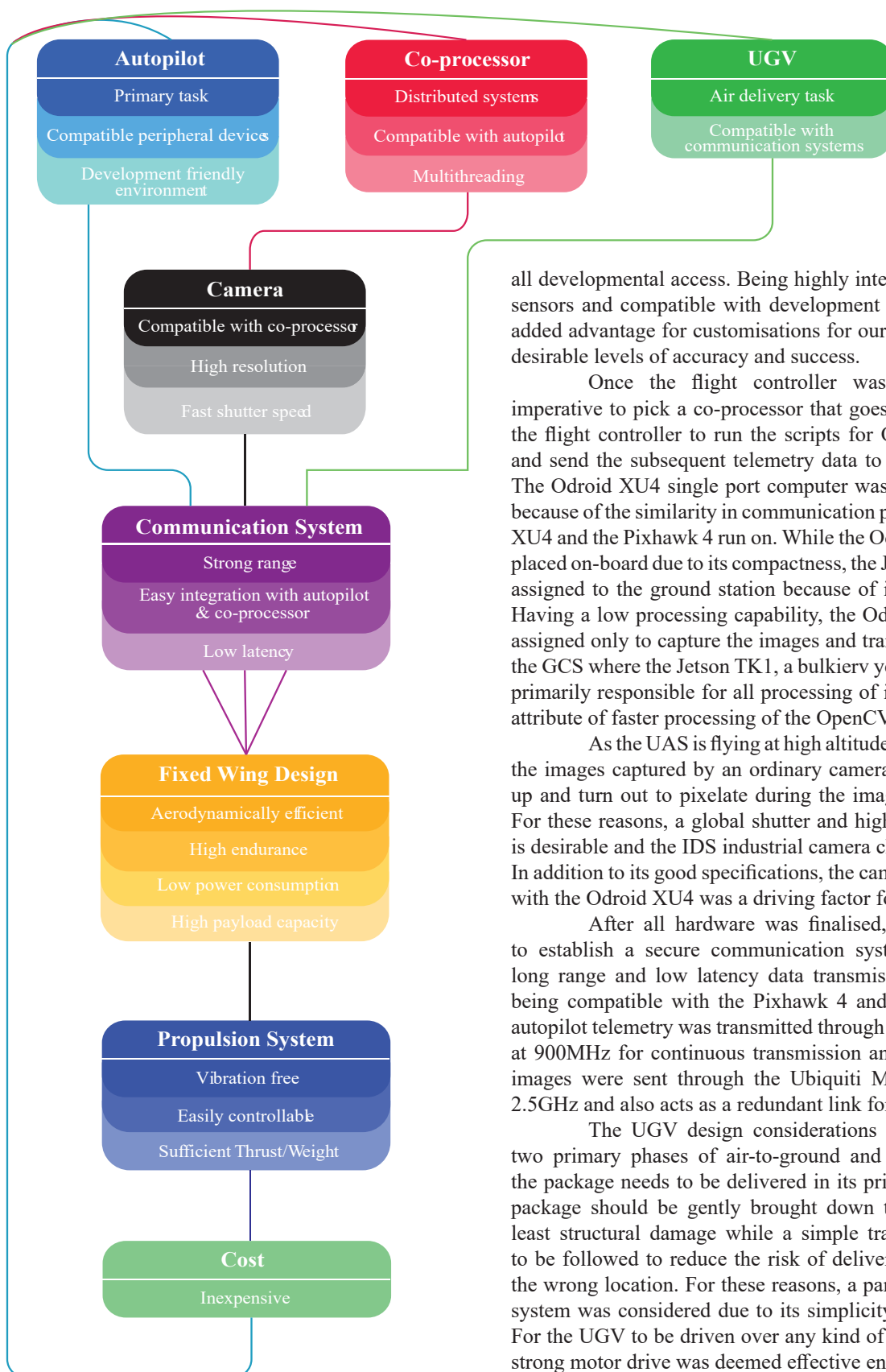


**Figure 2:** System requirement analysis flowchart

Selection of the flight controller is a prime aspect towards the fulfilment of the design rationale because of its influence over the Autonomous Flight and Obstacle Avoidance tasks which make upto 40% of the mission demonstration. Moreover, an incapable flight controller would hamper the overall performance and mission scores. The 3DRobotics Pixhawk is used because of its ease of implementation, teams experience with it and an open source platform providing the user with

all developmental access. Being highly integrable with various sensors and compatible with development boards provides an added advantage for customisations for our mission to achieve desirable levels of accuracy and success.

Once the flight controller was selected, it was imperative to pick a co-processor that goes hand in hand with the flight controller to run the scripts for Obstacle Avoidance and send the subsequent telemetry data to the ground station. The Odroid XU4 single port computer was shortlisted for this because of the similarity in communication protocols the Odroid XU4 and the Pixhawk 4 run on. While the Odroid XU4 has been placed on-board due to its compactness, the Jetson TK1 has been assigned to the ground station because of its size and weight. Having a low processing capability, the Odroid XU4 has been assigned only to capture the images and transmit the images to the GCS where the Jetson TK1, a bulkier yet powerful GPU, is primarily responsible for all processing of images owing to its attribute of faster processing of the OpenCV libraries.

As the UAS is flying at high altitudes and cruise speeds, the images captured by an ordinary camera would get blurred up and turn out to pixelate during the image processing flow. For these reasons, a global shutter and high resolution camera is desirable and the IDS industrial camera checks all the boxes. In addition to its good specifications, the camera's compatibility with the Odroid XU4 was a driving factor for its selection.

After all hardware was finalised, it was imperative to establish a secure communication system that ensures a long range and low latency data transmission in addition of being compatible with the Pixhawk 4 and Odroid XU4. The autopilot telemetry was transmitted through RFD900 operating at 900MHz for continuous transmission and low latency. The images were sent through the Ubiquiti Module operating at 2.5GHz and also acts as a redundant link for the autopilot data.

The UGV design considerations were based on the two primary phases of air-to-ground and ground drive. As the package needs to be delivered in its pristine condition, the package should be gently brought down to the ground with least structural damage while a simple trajectory is required to be followed to reduce the risk of delivering the package to the wrong location. For these reasons, a parachute deployment system was considered due to its simplicity and effectiveness. For the UGV to be driven over any kind of terrain with ease, a strong motor drive was deemed effective enough.

In addition to the newly added UGV payload, the rest of the electronic components make up at least 6kg of the takeoff weight. A fixed wing aircraft is highly efficient in carrying higher payloads over long distances while consuming less energy because of it being more aerodynamically streamlined in nature. Such an aircraft setup gives the UAS an added gliding time and higher endurance, which is necessary to complete the increased flying distance for the AUVSI SUAS 2019 in the minimum flying time possible.

A twin-motor electric propulsion system was



preferred over an IC engine due to the fact that motors are easily controllable and the thrust-to-weight ratio can be set in accordance to the different phases of the flight such as takeoff, turning, cruising, etc. This selection also came as a learning experience after the team equipped an IC Engine at SUAS 2018 and was unable to control the operating velocities at turns, that resulted in larger turning radii that lead to the geofence being crossed multiple times. Electric motors do not create any significant vibrations to the airframe thereby maintaining the aircraft's stability, while being noise and pollution-free that is an important aspect towards the implementation of such technology to the ecosystem in the longer run.

## 2. SYSTEM DESIGN

Figures 2 and 3 describe the flow of signal on-board and on the groundstation respectively

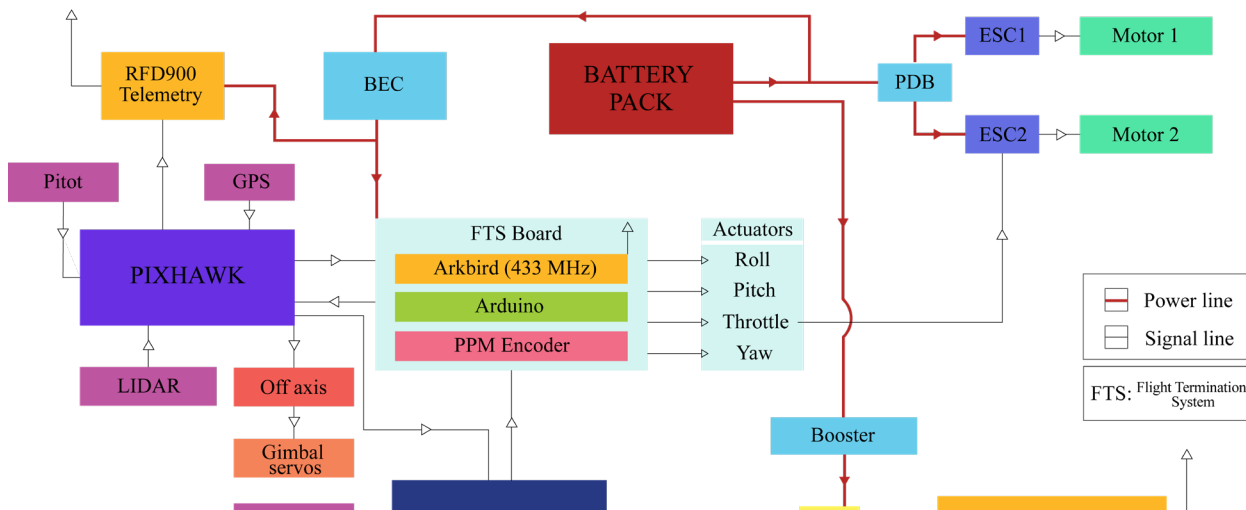


Figure 3: On-board system

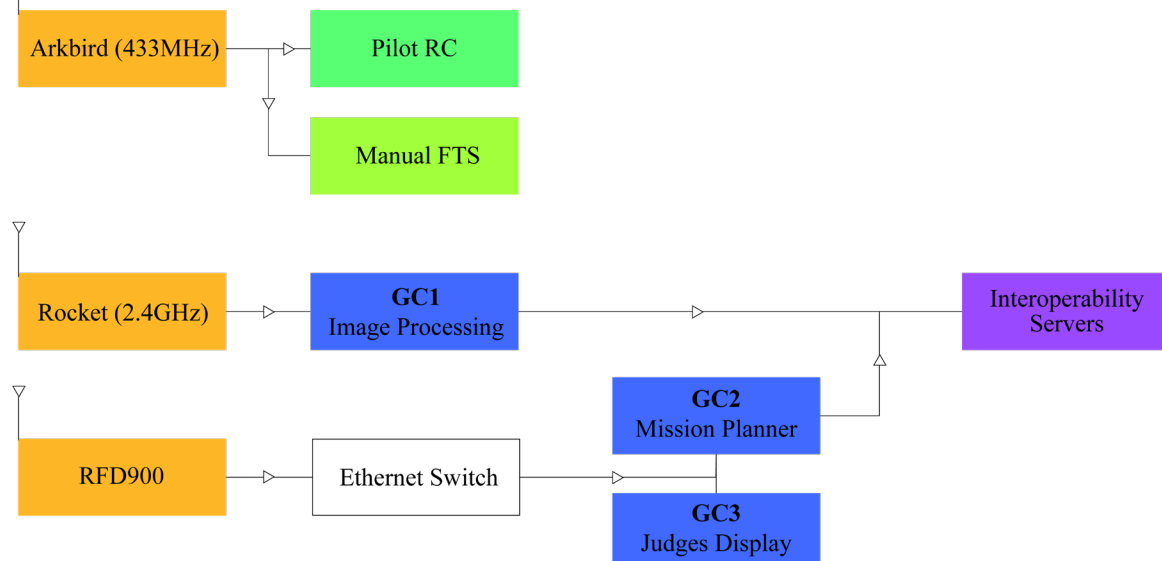


Figure 4: Ground Control System

### 2.1 Aircraft

#### 2.1.1 Design

The aircraft for SUAS 2019 was designed, while keeping in mind the stability required for the tasks like airdrop and object detection, while being equally maneuverable at all times, so as to avoid the emerging obstacles. Having to drop a UGV from the aircraft, the payload bay was designed to accommodate the biggest of payloads. The avionics section within the aircraft was also enlarged, for easy component placement and troubleshooting.

The budget was the biggest hindrance to the technological development and dictated the decision flow severely. Analysing the expenditure from the previous year, a cost benefit analysis was performed to understand the shortcomings while executing the work and measures have been taken this year to make the technology as cost-effective as possible. The UAS was developed keeping in mind the minimisation of material cost by reusing electronic components and consumables, performing test flights at nearby open fields to reduce cost of travel and indirect expenses and developing new in-house fabrication and testing techniques to reduce manufacturing and direct expenses.



single motor puller engine. Having a high wing configuration, thereby creating an aerodynamic dihedral effect, with an aspect ratio of 6.1 makes the aircraft laterally more stable, without sacrificing much of its maneuverability. Also, it provides a good clearance off the ground for the propellers.

In addition, Orca also has Hoerner Wing Tips, due to which the upper surface of the wings is longer than the lower surface, which causes the centre of the wing tip vortex to move far out from the tip edge, reducing the induced drag and the downwash intensity.

The aerofoil of choice is Curtis C-72, with the maximum camber of 3.8% at 50% of the chord, from the leading edge, and with a maximum thickness of 11.7% at 30% of the chord. In addition, the aerofoil thickness is increased by 25% of the original in order to get a thickness to chord ratio of 14.62% which increases the lift coefficient at low Reynolds number, without any significant increase in drag coefficient. Increasing thickness also increases the nose radius, as a result of which the wings get a gentler stall break since a higher airfoil nose radius keeps the boundary layer attached for longer due to a positive pressure gradient at the leading edge. A  $C_{L_{max}}$  of 1.62 and a  $C_{L_0}$  of 0.85 are achieved by increasing the thickness by 25% (an increase of 22% and 21.42%), which were originally 1.32 and 0.7 respectively. This also results in a max  $C_L/C_D$  of 131, which at original thickness was 118. So, by increasing the thickness we have gained a 11% increase in max  $C_L/C_D$ .

The Horizontal Tail is moderately tapered with a low aspect ratio in order to get a high-volume coefficient, thus improving the longitudinal stability which is accompanied by a long moment arm and high elevator deflections, which accounts for the quick pitching movement of the aircraft. In the case of, the directional control, the aircraft has a swept back Vertical Tail of moderate taper and aspect ratios in order to reduce the tail drag but at the same time, the aircraft has a high yawing rate due to its high deflection rudder, which makes it easily steerable even during turbulence.

The landing gear configuration on Orca is a Conventional type, the main reason for which is to provide a greater steering moment arm, so that the aircraft can make tighter turns on the ground. Also having a conventional configuration, would allow the aircraft to carry more weight

Performance	
Cruise Speed	15m/s
Max. Speed	22m/s
Min. Speed	12m/s
Min. Turn Radius	3.88m
Endurance	27 minutes
Thrust/Weight	0.75
Rate of Climb	7.87m/s

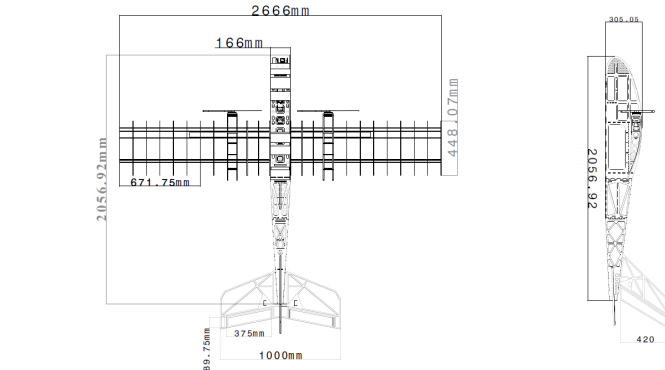


Figure 5: Schematic of Orca, with dimensions

on the main gear directly. Also the main gear allows for more reinforcing.

Orca receives its power from 2 MN-605S 320 KV motors from T-Motor, with 22-inch propellers in front of them. This combination produces a combined static thrust of 14.2 Kg at 6000 rpm.

A Flow Visualisation was useful in understanding the strong stagnation pressure zones on the surface of the aircraft and also to identify regions of turbulent flow around the airframe to further take steps of streamlining the body for reducing pressure and skin drag.

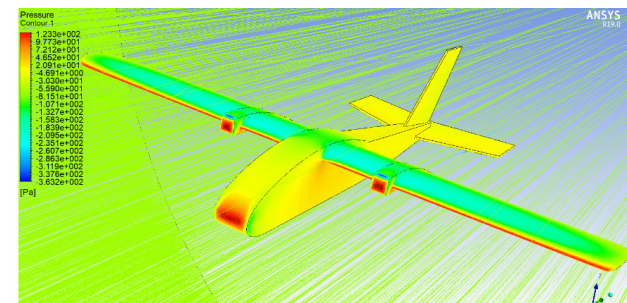


Figure 6: Static pressure contours of the 3D model of Orca

Table 1: Aircraft Design Chart and Performance Envelope

	Wing	Horizontal Tail	Vertical Tail
Airfoil	Curtis C-72 (125% thickness)	Flat plate (10mm)	Flat plate (10mm)
Span	2.68m	1m	0.4m
MAC	0.45m	0.35m	0.32m
Area	1.18m	0.35m <sup>2</sup>	0.128m <sup>2</sup>
Root Chord	0.45m	0.4m	0.4m
Tip Chord	0.45m	0.3m	0.24m
Aspect Ratio	6.1	2.85	1.25
Sweep Angle	0°	16.7°	38.66°
Taper Ratio	1	0.75	0.6

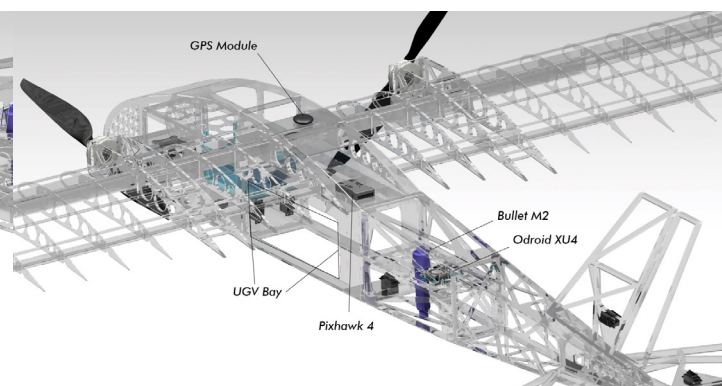
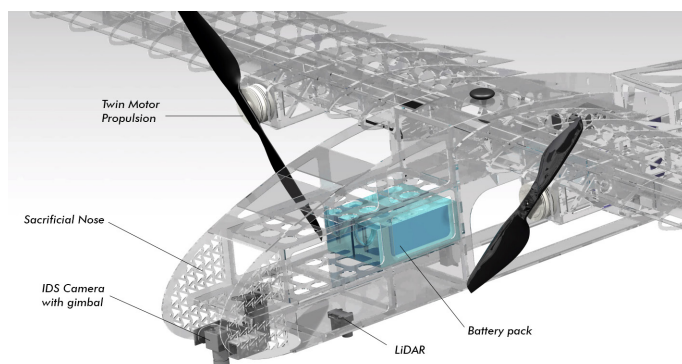
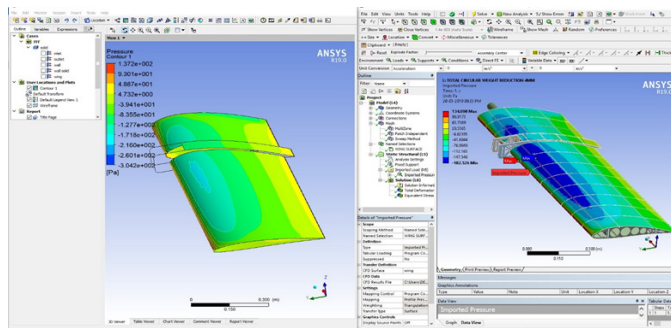


Figure 7: Internal view of Orca

### 2.1.2 Structural Optimization

Once the aerodynamic properties of the UAS were finalised, then began the rigorous process of structural optimization of the plane. The goal here being to reduce the weight of the UAS without compromising its strength. Initial stress analysis was carried out using Static Structural Analysis Workbench of CATIA V5 due to its user-friendliness, while more complex simulations such as one-way FSI and analysis of large assemblies was carried out using ANSYS 19.1. The parameters to compare various structural configurations was weight, Von-Misses stress, deformation and ease of fabrication.

As the pressure contour on the surface of the wing is not uniform, a fluid structure interaction (FSI) analysis was carried out using ANSYS 19.1, as shown in Figure 8. A total of



**Figure 8:** Fluid structure interaction creating pressure and stress contours over wing structure

30 wing structures were simulated and compared to determine spar material, spar internal diameter and external diameter, spar length, ribs' structure, number of ribs, number of stringers, shape of the forward and rear secondary spar (for example I-section, rectangular or cruciform etc).

The spar external diameter was estimated at 40mm and internal diameter at 36mm with a spar length of 1.5m. The shape of the rear and forward secondary spar are rectangular sections spanning the whole length of the wing. In the end about 522 gram of weight was reduced from the wings and 34% increase in strength was obtained with minimum deflection.

Hence, it was analytically found from the figures that the aerodynamic load or stress imparted by the aerodynamic pressure contours over the wing becomes constant after a spar length of 1400mm, shown in Figure 9.

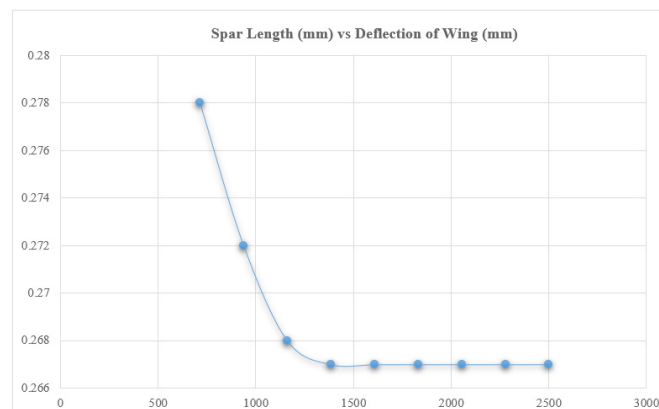


**Figure 9:** Aerodynamic stress deflection variation with spar length

The fuselage, empennage, vertical tail, Horizontal tail and landing gears were all subjected to various loading conditions, one of them is depicted in Figure 10. Stress analysis was carried out on total of 124 configurations of structures and 174 simulation conditions. Various parameters such as Von-misses stress, deformation, weight and strength to weight ratio were compared and evaluated for all the structures. Mass was added to critical areas which were subjected higher stress levels. For example, the Forward bulkhead has a thickness of

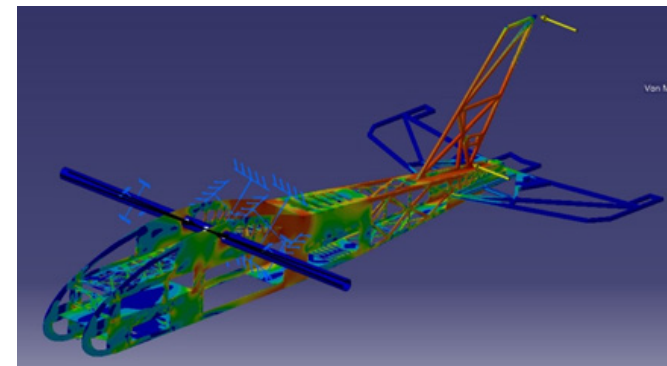


**Figure 10:** Stress analysis of empennage

about 6mm while the aft sections have a thickness of 3mm as the forward section of the fuselage houses the drop, wing junction, main landing gears and other electronic components such as batteries. Stress concentrations were reduced using fillets of appropriate radius. Stiffness of various areas were increased using stiffeners, bulkheads and other structural members. In the end, that structure was finalised which had acceptable level of strength to weight ratio. The total weight of the UAS excluding the wings was reduced from 7kg to 6.759 kg. while an increase in 32% strength of fuselage, 16% in empennage, 65% in vertical tail and 29% in horizontal tail were obtained.

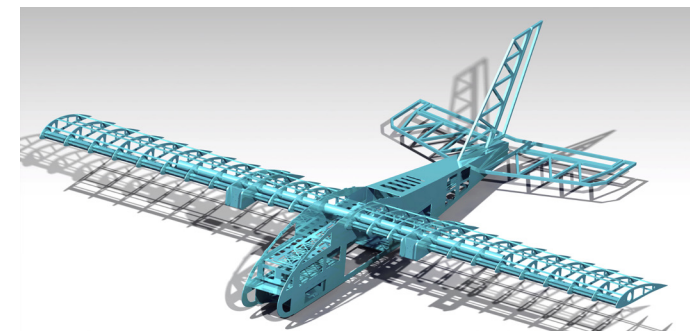


**Figure 11a:** Structure before optimization

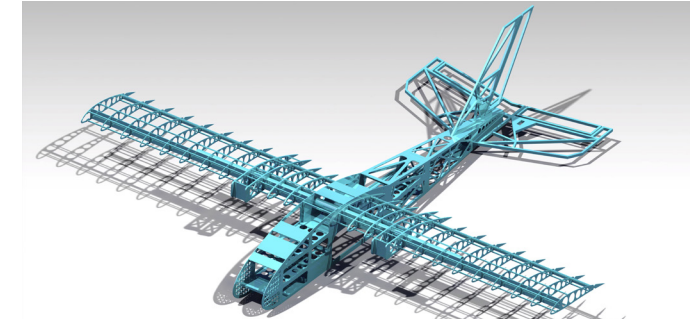


**Figure 11b:** Structure after optimization

### 2.1.3 Shock Dampening in Main Landing Gears

During aircraft landing, the landing gears experience various loads in an instant of time. The shocks are directly transferred to the aircraft structure. Hence reducing these forces during landing increases the redundancy and also the life of structure while achieving a smooth auto-landing. Various dampening techniques were tested in order to validate the system for the smoothest and safest landing experience.

To have an approximate value of the forces experienced during landing, an accelerometer was fitted into a demo landing model created using a base plate idealizing the belly plate of aircraft below which the different gear setups are provided. The accelerometer is placed over each gear and then the whole setup is run over a small bump to simulate a sudden shock. The accelerometer in mean time takes the acceleration readings it experiences against time. The data is then used to plot a graph of acceleration vs time using MATLAB.

The graphs in Figure 12 provide a basic comparison of accelerations in the system without and with suspension.

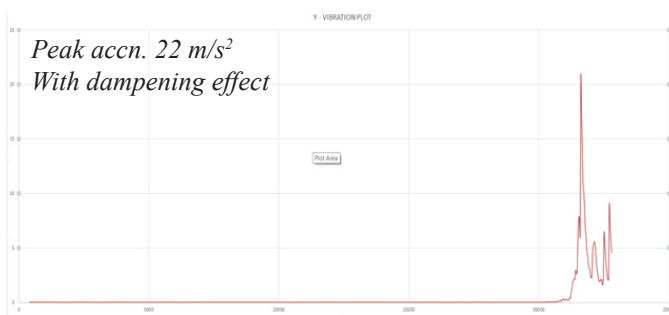
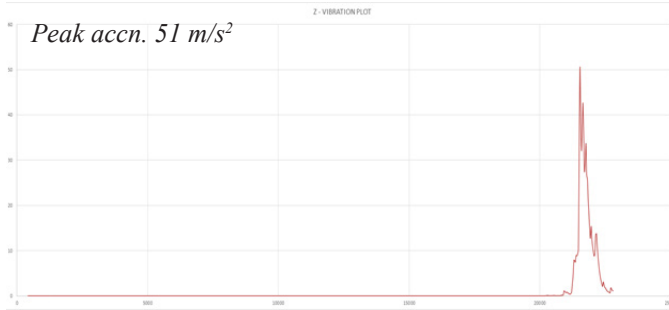


**Figure 12:** Dampening, with and without suspension

For our case studies, we have taken three systems;

1. Without suspension/rubber tires
2. With spring suspension (slow damp)
3. With pneumatic suspension (full damp)

After the second run, the graphs are shown in Figure 13.

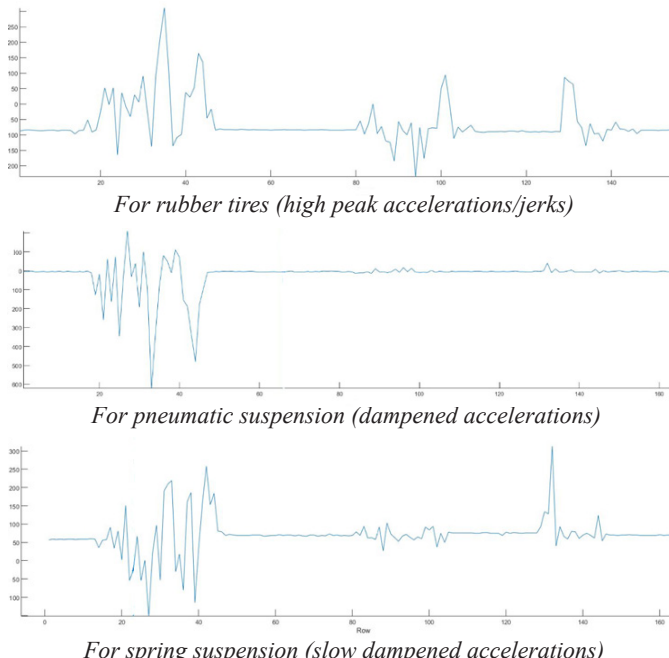


**Figure 13:** Comparison within various dampening setups

From the graphs, we could understand that the pneumatic suspension provided best shock absorbing properties for the given gear and has been considered for the landing gear setup.

#### 2.1.4 Static Stability

The graphs in Figure 14 depict the lift and moment coefficient variation of the UAV over a range of angles of attack respectively. As per calculations the  $C_L$  required at cruise velocity i.e 15m/s is 0.9, which is seen to intersect at an AoA of 3°. To make this the cruise/trim angle during flight, the horizontal tail is set at an incidence angle of -8°. With these design parameters the  $C_m$  vs AoA has a negative slope, thereby validating a good longitudinal static stability regime and a trim condition at 3° AoA. The graphs in Figure 15 represent the rolling and yawing moment coefficient of the UAV respectively. Both the graphs possess a slope which prove that the Orca is statically stable in the lateral and directional axes.

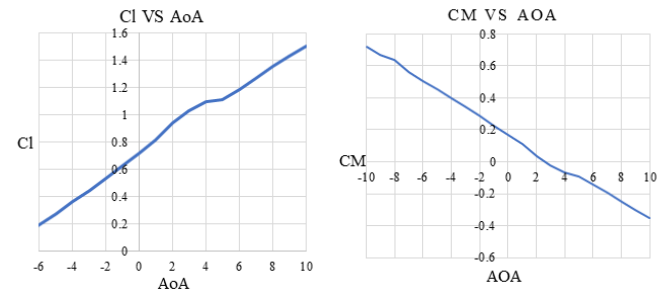


**Figure 14:** Static longitudinal stability

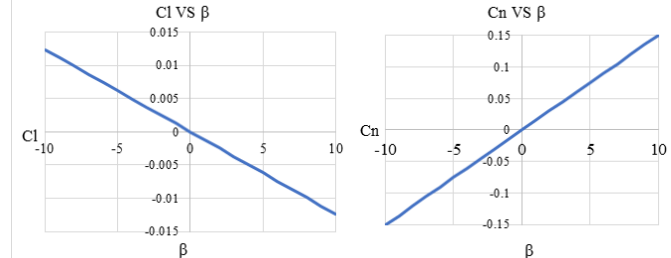


**Figure 15:** Static lateral & directional stability

## 2.2 Autopilot

The Autopilot is the heart of the UAS and will be responsible for all flight controls. As most our operations happen onboard, the flight controller is a low-level computer that works in coordination (depending on flight situations) with the higher level onboard computer which will assist the flight controller

Contrary to last year, the Pixhawk 4 was chosen as the Flight Controller for the aircraft this year. The Pixhawk 4 autopilot is a highly tested and reliable open-source system, a feature which is very important for its integration with our systems. The Pixhawk 4 has plug and play support for most of the sensors like the GPS, Lidar and Airspeed sensor, assisting in better autonomous flight.

It is a powerful flight control unit which uses isolated Inertial Measurement Unit (IMU) and Flight Management Unit (FMU), effectively reducing interference to sensors. It also contains a redundant IMU which enhances the safety and reliability of the system. The Extended Kalman Filter (EKF) algorithm has been used to estimate the vehicle position, velocity and angular orientation based on the IMU, compass, GPS, airspeed and barometric pressure measurements.

The selection of Pixhawk 4 was based largely on the following points:

1. Open Source, highly flexible and trusted autopilot
2. Abundant connectivity options for various sensors and peripherals
3. Integrated backup system for in-flight recovery and manual override via hardware (not involving any electronics)
4. Redundant power supply and automatic failsafe mechanisms.
5. Powerful Cortex M4F processor for running complex algorithms for stable flight dynamics and navigation.
6. Affordable.
7. Open-source Ground Control Station Mission Planner for programming all parameters, waypoints, geofence etc

For our testing, the Pixhawk 4 runs the ArduPilot 3.9 firmware. The ArduPilot firmware was chosen as it is the most popular firmware available because of its developer support, features and regular updates and patches.



**Figure 16:** Pixhawk 4



Ardupilot is capable of autonomous takeoff, waypoint navigation and autonomous landing. Thus, easing the team's effort in autonomous navigation.

The system is configured for an autonomous takeoff on the runway and after completion of the mission, safely land on the runway with the help of a well-tuned airspeed sensor, short-range laser altimeter (LiDAR) and GPS. The autonomous takeoff and autonomous landing was initially tested on our test airframe after which we were able to achieve accurate flare, takeoff distance and pitch angles.

The system was tuned for Roll and Pitch in Auto Tune mode as shown in Figure 17. The Auto Tune mode is a flight mode that flies in the same way as FBWA, but uses changes in flight attitude input by the pilot to learn the key values for roll and pitch tuning. While flying we were required to give sharp attitude changes so that the autotune code can learn how the aircraft responds. This was followed by manual fine tuning in FBWA mode wherein we adjusted the D value in order to improve the accuracy of the roll and pitch response and make the plane less affected by gusts and turbulence.

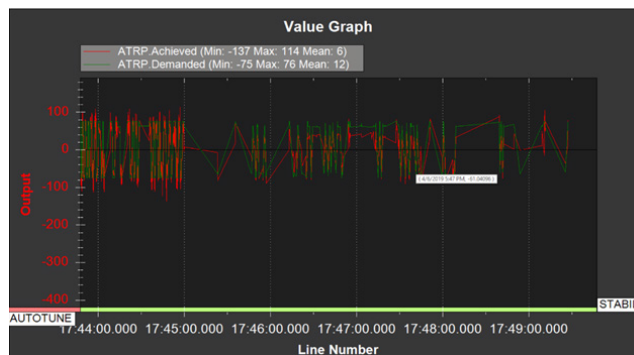


Figure 17: Autotune results

After receiving satisfactory result, accurate waypoint navigation was achieved. The parameter selection for the configuration of the autopilot was done in accordance with the performance and stability parameters of the aircraft, shown in Figure 18 and 19.

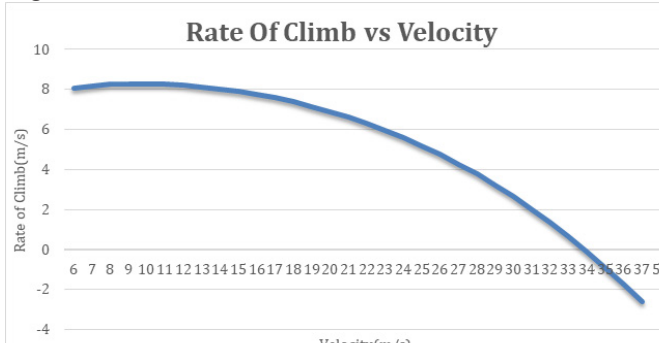


Figure 18: Performance graph

The calculated ground run is 38.04m for the aircraft to achieve takeoff. The Stall and Cruise velocities are 11 m/s and 15 m/s respectively. The maximum pitch angle of the aircraft is 30 degrees. Owing to the aerodynamically stable design, the maximum bank angle has been chosen to be 45 degrees.

Table 2: Comparison of Flight Controllers

Parameter	Pixhawk	Pixhawk 4
Waypoint Accuracy after Tuning		

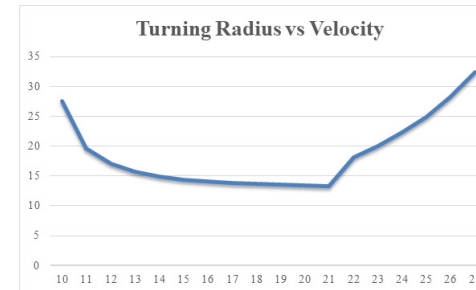


Figure 19: Performance graph

Table 2 consists of the results after tuning.

The L1 controller of the autopilot was tuned to achieve accurate waypoint tracking, the turning radius of the aircraft at cruise velocity at the maximum bank angle is calculated to be 24m, the mission waypoints and search grid were planned on this parameter, as the lack of inclusion of turning radius data during search-grid planning led the aircraft to go out of bounds and caused the team a considerable loss of points in SUAS 2018. Table 4 depicts the number of flights conducted on each test plane on different flight controllers.



Figure 20: Ground control station

### 2.3 Imaging Systems

As our system requirements in accordance to that of the competition were to:

1. Cover maximum area in a single frame to reduce the flight time.
2. High FPS
3. Wide range of aperture.
4. Customizable ISO.

Table 3: Camera Comparison

Name	Sensor Size (mm)	Resolution	Focal Length	Frame Rate	SDK Provided
GoPro Hero 7	6.17x4.63	4096 x 3072	35mm	10	No
UI-3860CP	5.61x3.175	1936 x 1096	25mm	4	Yes
ZCAM	17.3 x 13	4640 x 3480	20mm	2	Yes

IDS UI-3860CP was chosen after a careful analysis of various cameras in the market which suited our requirements. Easy to integrate with the SDK provided by the company helps to use certain performance parameters of the camera and take over control to a higher level.

Following are the factors of choice and specifications:

- Frame rate of 135 FPS
- Resolution of 1936x1096
- Ground Sampling Distance (GSD) of approximately 1.13 cm/pixel at 50 - meter flight altitude for a resolution of 1240x720. The resolution was chosen to suit the frame



Table 4: Waypoint capture on different airframes

Parameters	Test Plane 1		Test Plane 2		Competition Aircraft	
	Pixhawk	Pixhawk4	Pixhawk	Pixhawk4	Pixhawk	Pixhawk4
No. of test flights conducted	17	19	10	10	6	12
Waypoints Targeted	78	110	72	98	44	64
Waypoints Achieved	47	103	59	89	35	58

rate along with pre-processing.

- Wide aperture range of 1.6 to accommodate for varying lighting conditions
- Tamron 25mm 1/1.8" lens



Figure 21: IDS Camera

## 2.4 Object Detection, Classification and Localization

All imagery from the machine vision camera will be relay to NVIDIA Jetson TK-1 for processing using OpenCV (Cuda) and on Python 2.7.

Jetson TK1 was chosen, so as to have a compact onboard processing unit. But later was grounded considering the design and cost factor of aircraft while airborne.

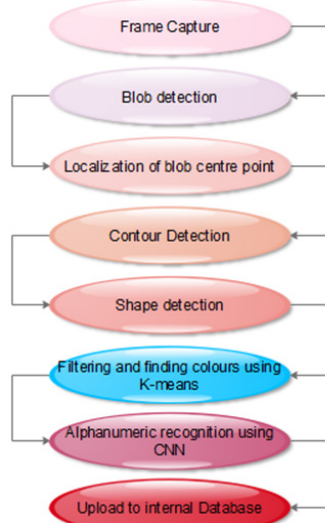


Figure 22: Object detection and classification flowchart

### 2.4.1 Blob Detection

Blob detection aims to detect regions that differ in properties, such as brightness or colour. Suitable blobs are detected and stored for further processing.

A series of filters (gaussian blur , erode , Dilate) and transformations are applied and the derived output is run through the canny transform for contouring the bounds and recording targets.

Same Blobs will be detected in the consequent frames, this

gives us redundant data points to recognize the true positives. False detections mostly are unique and rarely show up more than 1 – 2F times . More over the distance/orientation travelled by the aircraft is matched in order to qualify redundant targets.

### 2.4.2 Localization

Detected blobs are labelled with their respective location by calculating their offsets considering the image centre as the current location of the vehicle.

### 2.4.3 Contour Detection

The blobs are manipulated for processing using a custom algorithm. Manipulations are made to highlight the most abundant colours to define edges along coloured objects. The contours are extracted after certain specific transformations, giving the ability to work around with the shapes data points.

### 2.4.4 Shape Detection

Contour approximation is used to find the corresponding edges. Contour approximation is predicated on the assumption that a curve can be approximated by a series of short line segments. This leads to a resulting approximated curve that consists of a subset of points that were defined by the original curve. Additional cases of vertices and angular approximations were required for recognition of special shapes.

Further geometric parameters like circularity, convexity, etc. to verify for certain shapes. The angular array formed by shape vertices is also sorted and verified for shapes.

Multiple verifications and tests approve for the category of shape, Hence getting the required object.

Such methodology was chosen due to its simplicity and accuracy in recognition of the desired class.

### 2.4.5 Filtering and Finding Colours

The blobs so detected are cropped and passed through the k-means clustering function. Hence providing an output with the abundant colours as per the number of clusters. Hence classifying the background and alphanumeric colour to the degree of abundance respectively.

### 2.4.6 Recognizing Alphanumeric Character

Convolutional Neural Network is used to detect the corresponding alphanumeric character. The neural nets are trained using the synthetically generated dataset. The dataset is labelled systematically and trained extensively to attain maximum accuracy. TensorFlow is used as the backend. Alternatively, the OCR is passed on to the Tesseract-OCR engine. Multiple images of the same , oriented in different angles are passed on and processed parallelly to save processing time. The result is then fetched for the nearest alike members among the oriented images. This gives us the region of orientation and hence orientation is achieved.



#### 2.4.7 Selection of Best Sample

After termination of scanning of the search area, targets partially queued in the system for processing, after which the targets are then compared to sort the same objects and score the similarities. Scoring is based upon a standard, set up by our team with on-going testing. The categorical scores change with respect to the performance of the individual subsystems.

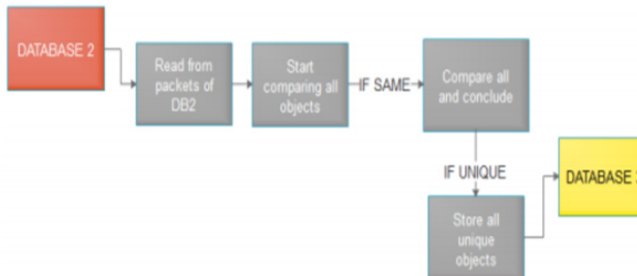


Figure 23: GUI Figure 1

#### 2.4.8 Target Selection

The targets hence processed are finally iterated through the GUI for the operator to inspect and conclude submission of targets autonomously. In case of any discrepancies, the operator can override to manual submission of targets.

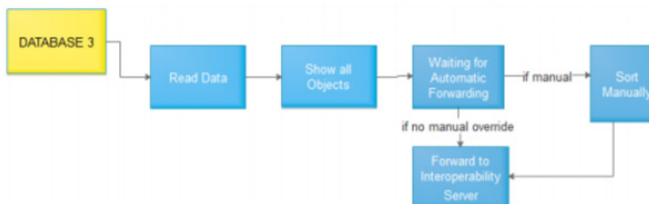


Figure 24: GUI Figure 2

#### 2.4.9 GUI

For Monitoring processes and conclusions made autonomously, we have introduced a custom GUI for Ease of Operations. The sorted objects can be seen live and can be altered if needed. If no Manual override takes place, the software will autonomously finalize targets and send them to the Interop-Server.

In case of any manual override, the software will be used to edit data for targets and Images for passing it onto Interop Server. The GUI has a built-in image editing tool and data editor right in place for ease of use. The operator needs minimal of knowledge to operate the Imaging System.

Figure 25: GUI Flowchart

Table 5: *ODCL Results*

Processing Phase	Confidence	Samples Tested
Shape recognition	93%	28/30
Colour recognition	86%	43/50
Character recognition (LSTM)	82%	41/50
Character recognition (KNN)	78%	39/50
Character recognition (Tesseract)	88%	44/50
Orientation	63%	38/60
Final Target	47%	14/30

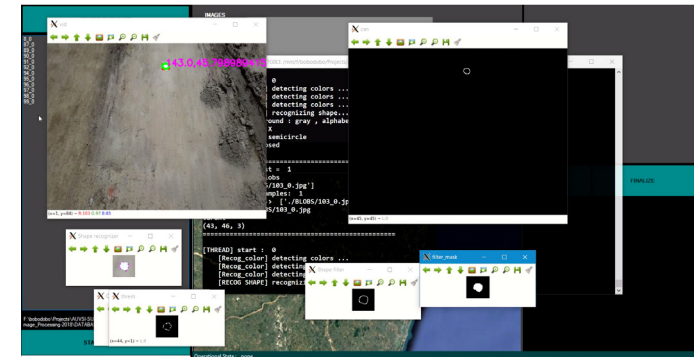


Figure 26: Object detection & localization

#### 2.4.10 Gimbal

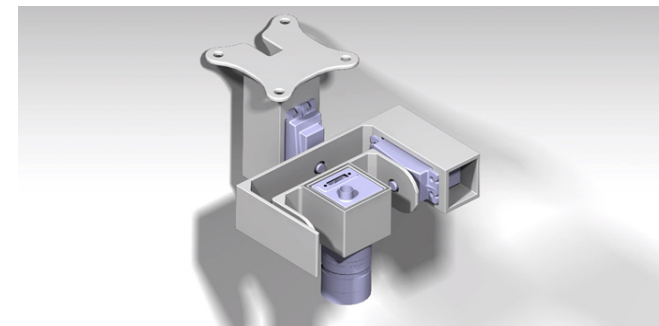


Figure 27: Gimbal

For stabilized images a gimbal mechanism has been developed as shown in Figure 27. The image stabilisation is being taken care by a 2 Axis Gimbal System, which will stabilise our imaging system about the Roll and Pitch Axes. It comprises of three distinct 3D printed parts as the structure and two Savox servo motors for actuation. The gimbal will be mounted, in the nose of the aircraft. The gimbal is capable of providing a max Field of View (FOV) of 130o Degrees, along both the axes.

#### 2.4.11 Off-Axis

An off-axis algorithm was developed to capture the emergent object. The gimbal's stabilisation will be done with the help of ArduPilot's feature of gimbal stabilisation. We are using a 2-axis gimbal which is operated with the help of 2 Savox 1256-TG servos.

The off-axis task will be accomplished by using an intermediate Arduino between Pixhawk and the gimbal. We will be using the gimbal outputs of the Pixhawk to stabilise the gimbal. During the off-axis task, the Arduino will take the PWM outputs from Pixhawk, add the calculated offsets and send that to the gimbal's servos. The offsets are calculated in real-time by the intermediate Arduino according to the UAV's position and heading.

The latitude and longitudes are first converted to radians and put into the following formula:

$$\text{bearing} = \text{atan2}([\sin(\text{longitude}_2 - \text{longitude}_1) * \cos(\text{latitude}_1)], [\cos(\text{lat}_1) * \sin(\text{lat}_2) - \sin(\text{lat}_1) * \cos(\text{lat}_2) * \cos(\text{longitude}_2 - \text{longitude}_1)])$$

This bearing is converted to degrees.

The yaw can be calculated with the following formula:

$$\text{yaw} = \text{vehicle's heading} - \text{bearing}(\text{latitude}_1, \text{longitude}_1, \text{latitude}_2, \text{longitude}_2)$$

To calculate the roll, we use the following formula:

$$\text{roll} = \text{atan} \left( \frac{\text{distance of target(feet)}}{\text{height(feet)}} \right)$$

#### 2.4.12 Aperture

Last year we flew our UAV when the sun was setting and faced a new problem of proper aperture position as the sunshine was reducing minute by minute and our camera could not capture clear images. In order to obtain the best images in the given conditions an “Automated Aperture Adjustment System”



**Figure 28:** Automated Aperture Adjustment System

has been designed and developed which uses computer vision to determine the amount of light the camera's sensor needs and automatically adjusts the aperture. The aperture is adjusted by using a 9-gm servo linked with the camera by a "Crank Rocker Mechanism", a four-bar inversion where servo horn acts as crank and aperture horn as rocker.

Hence, an angular change in the servo horn produces angular change in the aperture. The horn used at the aperture is 3-D printed as per the design requirements.

This system removes the reliance on human intervention to set the aperture and works in conjunction with image processing sub-system for a better performance.

## 2.5 Obstacle Avoidance

The algorithm that SRM UAV developed for Orca takes the latitude and longitude of waypoints as well as the obstacles and converts them into UTM in order to use them as cartesian coordinates. To check whether the obstacles are obstructing the path of the UAV, intersection points between the obstacle (circle) and the current trajectory (first waypoint to second waypoint – line) are computed. If the obstacle is indeed obstructing the UAV's path, a small detour is planned to use the intersection points and the midpoint of the shorter arc(in order to minimal change in original trajectory) formed by the intersection points and the obstacle(circle). The detour waypoint will be set at a distance that considers the turning radius of the aircraft at that particular velocity such that the turning radius of the aircraft is greater than the radius of the obstacle. The coordinates are then converted back into latitude and longitude and then fed into the UAV's flight plan in order to execute the new computed trajectory.

Limitations:

- In case there are multiple obstacle close to each other, the current algorithm won't be able to find an optimized path.

Solution:

- Consider the group of multiple obstacles whose distance between each other is less than a certain threshold as a circular blob.

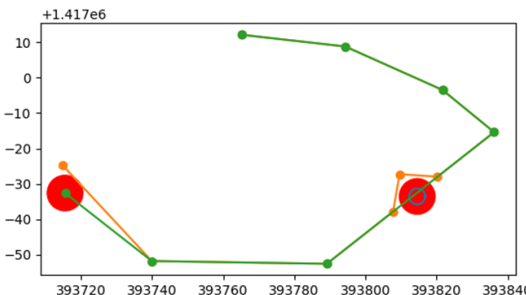


**Figure 29:** Obstacle avoiding trajectory

**Table 6: Obstacle Avoidance Results**

Number of obstacles tested against	45
Number of obstacles avoided	37
Accuracy Percentage	82.22%

## 2.6 Communication Systems

### 2.6.1 Aircraft Communications

The Orca has 3 communication links as shown in Figure 30. The main pilot RC signal link is operated at 433MHz FHSS frequency, a simplex link from ground station pilot to the aircraft. The RC link uses a DX8 transmitter and an Arkbird repeater module to increase the transmitted power and range. The Arkbird module uses an omnidirectional 5-dBi whip antenna both on-board and ground station allowing the pilot to send signals to the aircraft irrespective of its orientation. The autopilot telemetry uses an RFD900X telemetry module with a pair of dipole antenna to send and receive autopilot data operated at 902-928 MHz frequency band compared to last years Ubiquiti module, thereby maintaining a continuous link and making the system redundant. The Ubiquiti M2 module is used to send and receive imagery and data from on-board computer. The Bullet M2 is used on the aircraft with a 5-dBi omnidirectional dipole antenna and Rocket M2 on the ground station with a 16-dBi sector antenna to increase the directivity and range of the data.

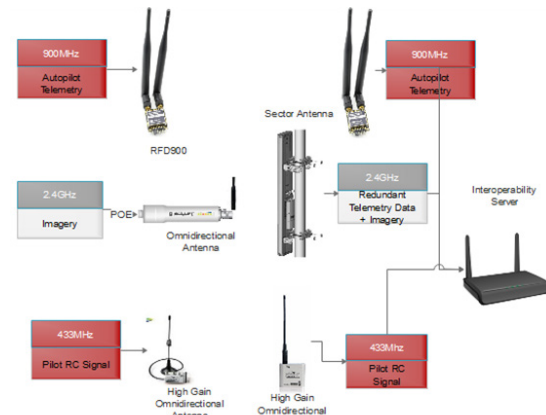


**Figure 30:** Communication systems block diagram

Range and latency test were conducted on all communication links to validate the use of above-mentioned communication modules. The range of Arkbird module with the chosen antenna was found to be of 5km LOS and the Ubiquiti was found to be of 2.5km LOS which suits our mission requirements. Latency tests were conducted between Ubiquiti Bullet M2 and Rocket M2, the graph of which is depicted in Figure 31.

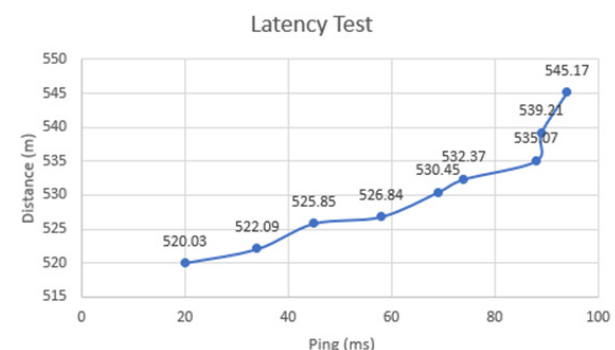


**Figure 31:** Latency test of Ubiquiti

Due to improper image quality received last year at the competition site, latency tests were conducted. The results depicted that the lag in data reception increases with distance, hence demanding a proper image buffer management.

The antennas were placed outside the aircrafts to maximize the reception of the signal from the ground station and away from all electronic components to avoid magnetic interferences.

### 2.6.2 UGV Communications

The unmanned ground vehicle (UGV) is equipped with Hope RFM95W LoRa modem operating at a frequency of 915 MHz.



The range with a 2-dBi dipole antenna was found to be 1km in LOS which suited our requirements. Abiding to the weight constraints of the UGV, a lightweight, compact, long range and cost effective module was required due to which the LoRa module was chosen above other telemetry modules.

The communication system is summarized in Table 7.

**Table 7: Communication System**

Link	Frequency	Module	On-board Antenna	Ground Station Antenna	Direction of Link
Pilot RC control	433 MHz	Arkbird Repeater	5-dBi Whip	5-dBi Whip	Uplink
Autopilot Telemetry	902-928 MHz	RFD900X	3-dBi dipole	3-dBi dipole	Uplink & Downlink
Imagery & On-board computing	2.4 GHz	Ubiquiti Bullet M2 & Rocket M2	5-dBi dipole	16-dBi sector	Uplink & Downlink
UGV	915 MHz	LoRa RFM95W	2-dBi dipole	2-dBi dipole	Uplink & Downlink

### 2.6.3 Antenna Tracker

The design of the tracker has been made efficient to the maximum by using industry grade aluminum that is easily available and also taking into account its cost effectiveness compared to other materials. The design of the antenna tracker has been made such that there is least interaction between the aluminum frame and the directivity of the antenna in order to maintain maximum signal strength. The tracker is mounted on a 2-way axis driven shaft which has been mounted on two 2inch aluminum plates for more strength and stability due to the weight of the Ubiquiti module. The 2-way axis mechanism provides a much larger coverage of the UAS by covering the horizontal as well as the vertical components where the UAS is being flown and the orientation of the tracker changes accordingly. For the rotary shaft of the tracker, a 360 degree rotation freedom has been structurally implemented for easier access to track on the ground such as during takeoff and landing. Structural notches and holes were made in order to reduce the overall weight of the tracker assembly as well as maintaining its structural integrity and ruggedness. For the rotation of both the shafts, 2 HS-5685MH Servos were used which are heavy duty servos and provide the required amount of torque which is necessary to move the aluminum structure efficiently.

## 2.7 Power Systems

### 2.7.1 Flight Time Calculations

To overcome the shortcomings of an IC engine propulsion system, an electric propulsion system was selected. Subsequently, the batteries were selected keeping the mission time in mind. The flight time obtained from these batteries is,

- Maximum Current draw on which calculation is based: 120A (Found out by Unit Testing + 20% margin)
- Battery capacity: 32000mAh

$$\frac{\text{Battery capacity}}{\text{Total current draw}}$$

$$\frac{32000\text{mAh}}{120\text{A}} \times 60 = 16 \text{ minutes}$$

- Maximum current draw: 60A
- Flight time for the aircraft:  $\frac{\text{Battery capacity}}{\text{Total current draw}}$

$$\frac{32000\text{mAh}}{60\text{A}} \times 60 = 32 \text{ minutes}$$

Average Flight Time will vary from 16 to 32 minutes based on the throttle.

### 2.7.2 Flight Termination System

The Flight Termination System is designed as per the specifications mentioned in the problem statement and other major risks that might endanger the aircraft, lives or property on the ground. The system is designed in-house and custom fabricated, as shown in Figure 20. It also acts as the power distribution system for the actuators of the aircraft. FTS is activated if any of the following conditions occur:

- RC signal loss
- Telemetry signal loss
- Manual FTS request
- Apart from FTS, warning systems to warn the ground station have also been incorporated in the system. These are:
  - Soft Geofence
  - Autopilot Failure

There is exclusive communication channel for the pilot to override in such cases to achieve complete manual control over the aircraft. On Communication loss:

- The aircraft will wait for 30 seconds to regain communication link.
- If communications are not regained, it will initiate return to land (RTL).
- After 3 minutes of communication loss, the FTS will terminate the flight.

## 2.8 Air Delivery

### 2.8.1 UGV Design

The team has designed and developed an Unmanned Ground Vehicle. The team worked on such a system for the first time, the major problem we encountered was how to land such a heavy object without compromising its structural stability and to also make it drive after the landing. The team designed and prototyped three concepts with different propulsion, and drive systems and configurations, shown in Table 8.

**Table 8: UGV Design Comparison**

Type	Drive Type	Fabrication material	Advantages	Disadvantages
Symmetric UGV	Rear wheel drive	Aluminium & ABS	Can land on top & bottom	Heavyweight
Skid type	Co-axial horizontal propulsion	Aeroply & PLA	Can land in any orientation	High friction & big size
Chosen Model	Diagonally opposite motors	Carbon fibre & sheet metal	Lightweight & small	Parachute required

The chassis of the UGV is casted with Carbon Fibre which keeps it lightweight and provides the required strength. The drive positioning of the UGV is quite uncommon but we have managed to cut down the width of the UGV by 31% of a similar UGV with motors positioned at the rear or

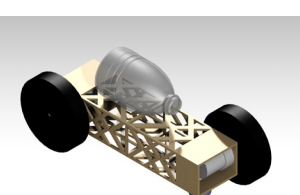


**Figure 33: UGV**



front as per our system, reducing the size and weight of both the UGV and fuselage (as the UGV fits inside the fuselage).

## 2.8.2 Parachute

After careful considerations, a parachute setup was finalised considering its simplicity and effectiveness.

The aerodynamics of any parachute is an important aspect for its design that govern the rate of inflation of the parachute, rate of descent and drag characteristics, all of which need to be considered for the mission. A high drag coefficient is highly desirable for the mission to provide a very low descent rate while a high rate of inflation is equally desired to achieve peak drag at the earliest and start the unaccelerated descent phase as soon as the UGV is dropped from the airframe in order to ensure a safe and stable landing. Various parachute configurations were then experimentally analysed for the best drag coefficient and rate of inflation. Firstly, a vented (10% total area) and non-vented parachute were tested for drag coefficient variations with respect to time. The prototype parachutes were tested horizontally in front of an open jet and drag was estimated with the help of a weighing scale that was attached to the parachute tether at a fixed wind speed. A rectangular block was placed at the mouth of the open jet that behaved as the UGV body and created a wake similar to that in the actual case. This block setup was important as the wake created by the UGV will reduce the efficiency of the parachute. Once the vented and non-vented configurations were compared, it was found that the parachutes vented at the apex had a higher drag coefficient than their non-vented counterparts as shown in Figure 33a. This leads to the inference that a vent allows the trapped turbulent air inside the parachute to escape thereby making the flow more streamlined with a higher Reynolds number and increasing the overall form drag over the face of inner side of the parachute. Moreover, a vent leads to a choked flow regime that not only causes a more uniform pressure distribution inside the parachute that increases static stability, but also leads to the formation of a low-pressure region behind the vent outside the parachute. This low-pressure region causes the parachute to bulge thereby creating a more curved 2D cross section for higher drag.

As a vented configuration was found to have a better bluff body aerodynamic performance, three different vented configurations were tested in the same way. Single dome, triple-dome and cruciform configuration parachutes, all vented, were compared due to high drag coefficients that can be attributed to their cross-sections. The vented cruciform parachute configuration was found to have the highest rate of inflation as it reached its peak drag at a rate of 18.0504 N/sec while having a high peak drag coefficient of 0.417, comparable to the other configurations, as shown in Table 9

**Table 9: Parachute Configuration Comparison**

Configuration	Peak $C_d$ coefficient	Rate of Inflation (N/sec)
Vented Dome	0.428	14.343
Vented Triple Dome	0.41	17.647
Vented Cruciform	0.418	18.0504

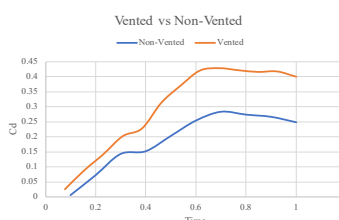


**Figure 34a: Vented vs Non-vented**

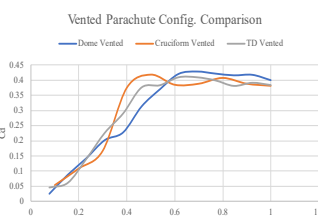


**Figure 34b: Vented Parachute Comparison**

## 2.8.3 UGV System Design

The UGV consists of an accelerometer to identify the sudden jerk upon landing to activate the UGV. The UGV waits until communication between the UGV and the ground station is established. The wheel drive is driven by 2 Brushed DC Motors with 60 RPM to overcome the torque required.

The motors are driven to the destination point by motor driver controlled by low level development board chosen such that it suits according to our requirements without unnecessary overhead calculations. Arduino Mega 2560 integrated with a GPS and a magnetometer was used to drive the UGV to the desired drop waypoint. Feedback algorithms were implemented to reorient the UGV and free from errors. The Mega is connected with a LoRa module which communicates with the ground station at 915 MHz. The UGV is terminated under 3 conditions :

- If the UGV reaches the destination coordinate, thereby completing the mission
- If the UGV crosses the geofence
- If the UGV does not communicate until 30 seconds of communication loss.

Figure 34 shows the system diagram for UGV.

## 2.9 Cyber Security

Cyber security is an important aspect in distributed systems where multiple computers are connected over a common network to exchange data. In such systems each computer is vulnerable to an external threat in the form of network breaches and unauthenticated access. Hardware has been selected considering secure protocols to avoid breaches. The following design pattern has been followed to ensure maximum security of all the subsystems.

**Table 10: Cyber Security & Communication Risks**

System	Potential Risk	Mitigation
Telemetry (RFD900)	Jammering, interference, & snooping	FHSS to prevent interference and jamming. AES encryption used to prevent snooping
WiFi (Ubiquiti)	Unauthorized entry into the network	WPA-2 used to protect the network
RC (TX & RX)	Jammering, interference, & snooping	FHSS is used to prevent interference and jamming. DSMX protocol used to prevent adversaries from gaining control of the UAV's RC systems
APIs	Unauthorized access	Authorization tokens are used to prevent unauthorized access
OBCs (Odroid XU-4)	Unauthorized access	SSH keys are used to prevent unauthorized access



### 3. SAFETY RISKS & MITIGATION

The application of the UAS being towards end user delivery service, safety of property, lives and the technology is the most important aspect of the overall mission. Various precautions and measures have been practised by each member of the team during the development of the UAS and protocols have

been prepared that are to be followed during the failures of any subsystem during the mission. Multiple simulations of the mission day scenarios have been performed and the following tables illustrate the safety management techniques that have been followed:

**Table 11: Mission Risks & Mitigation**

Safety RisksI	ndication	Consequences		Reduction Measures		Operator
		Local	Cascading	MitigationP	revention	
Autopilot Failure	<ul style="list-style-type: none"> <li>• Deviating largely from waypoints</li> <li>• Unexpected altitude behaviour</li> </ul>	N/A	Large deviation from flight plan	Manual override & switching back to auto	Activation of FTS or land	Pilot & Autopilot GCS personnel
RC-link loss	Loss of pilot control	Sudden maneuvers on short RC loss	Full RC link loss leading to crash	Activate redundant RC link over RFD900	Activate FTS to minimize crash hazard	Pilot & Communication system personnel
Autopilot Telemetry Loss	Improper data obtained on the ground station	Leads to false implications	Unsafe to fly with complete garbage data values	Activate redundant telemetry values over Ubiquiti	Antenna tracker installed for wireless communication	Autopilot personnel
Imagery Link	Dark images	False results after processing	Failure of ODCL mission	Images put in buffer and resend after regaining link	Process images captured on-board after landing	Imaging system personnel
Geofence Breach	<ul style="list-style-type: none"> <li>• Long turning approaches near the geofence</li> <li>• Aircraft going out of visibility</li> </ul>	Increase in unnecessary mission time	Loss of points & consequently leading to aborting the mission	Parameters set according to aircraft operating parameters	Soft geofence & software watchdog developed to alert the GCS	Distributed systems personnel
Low Battery	<ul style="list-style-type: none"> <li>• Low throttle values</li> <li>• Decrease in altitude</li> </ul>	Decrease in endurance	Crash or mission abortion	Land & replace batteries	Reserve power supply to take-over	Power system personnel
Steerable Landing Gear Failure	Unnecessary yaw during taxi	Improper auto take-off leading to misalignment of aircraft	Banking of aircraft during take-off thereby crashing into flight line	Immediate manual takeover & manual take-off	Proper landing gear mounting prior to flight & multiple taxiings	Pilot & mechanical personnel
Pilot Error	Low confidence & lack of decision making	Disturbing the harmony of flight line	Lack of control over the aircraft	Co-pilot for assistance	9 hours of sleep prior to flight	N/A

**Table 12: Developmental Risks & Mitigation**

Development Risk	Mitigation
<i>Test flights in cities pose a safety risk to people on the ground</i>	All test flights are conducted at a private airfield with no habitation in the surrounding areas.
<i>Personnel hazard while operating power tools</i>	Concerned members are required to wear safety goggles and gloves while using power tools. Moreover, proper training from university labs is provided to avoid any mishaps.
<i>Power issues to the flight controller</i>	Redundant Power supply using Power Module, Servo rail and USB.
<i>Loss of power at the ground station</i>	The ground station is powered by a UPS
<i>Injury due to misunderstanding of complicated and high-risk components</i>	Integration of hazardous and high-risk parts such as propellers and Li-Po batteries only at the end of the development process, with proper safety equipment and qualified member supervision
<i>Fabrication Errors</i>	<ul style="list-style-type: none"> <li>• Verifying the design after fabrication</li> <li>• Minimizing the human error by using precision machines.</li> <li>• Including the tight tolerances in design</li> </ul>
<i>Accidental arming of throttle on ground</i>	<ul style="list-style-type: none"> <li>• All team members are supposed to stand behind the wing after connection of battery.</li> <li>• 2 step arming of throttle. Physical safety switch and Software arming</li> </ul>

### 4. CONCLUSION

SRM-UAV has successfully developed an aerial platform to achieve the rationale of AUVSI's SUAS 2019. The ORCA has been engineered with utmost passion and care and tested for high standards of success, accuracy and safety learning learning from the previous experiences that the team has endured. SRM-UAV cannot wait to validate its tech at Maryland this June.